Supporting Information

An Organometallic $Fe_2(\mu\text{-}SH)_2(CO)_4(CN)_2$ Cluster Allows Biosynthesis of the [FeFe]-Hydrogenase with only the HydF Maturase

Yu Zhang,[1†] Lizhi Tao,[2†] Toby J. Woods,[1] R. David Britt[2*] and Thomas B. Rauchfuss[1*]

[1]School of Chemical Sciences, University of Illinois at Urbana–Champaign, Urbana, Illinois 61801, USA

[2]Department of Chemistry, University of California, Davis, California 95616, USA

[†]Y. Z. and L. T. contributed equally to this work.

*Corresponding Authors: *rdbritt@ucdavis.edu* and *rauchfuz@illinois.edu*

This PDF file includes:

Materials and Methods

Materials. Synthetic manipulations were carried out using standard Schlenk line and cannula techniques or in an MBraun inert atmosphere drybox containing an atmosphere of purified nitrogen. Operations were conducted at room temperature unless otherwise indicated. Solvents for air- and moisture-sensitive manipulations were dried and deoxygenated using a MBraun Solvent Purification System and stored over 4 Å molecular sieves. Iron pentacarbonyl (Sigma Aldrich), $K^{13}CN$ (99%, Cambridge Isotope Laboratories, Inc.), iron dodecacarbonyl (Strem Chemicals) and 18-crown-6 (99%, Oakwood chemical) were purchased from commercial sources. For the synthetic procedures, solvent volumes are approximate. Workup routinely entails rinsing products with antisolvent and drying under vacuum.

Physical Measurements. ^{1}H and $^{13}C\{^{1}H\}$ NMR spectra were recorded on Varian UNITY INOVA 500 MHz, Varian Inova 600 MHz and Bruker Ascend 600 MHz spectrometers. All chemical shifts are reported using the δ scale (ppm) relative to $SiMe_4$ using ^{1}H (residual) chemical shifts of the solvent as a secondary standard. Coupling constants (*J*) are reported in Hz. Data were collected at room temperature (RT) unless otherwise indicated. Elemental analysis was performed by the School of Chemical Sciences Microanalysis Laboratory utilizing a Model CE 440 CHN Analyzer. Cyclic voltammetry measurements were conducted under nitrogen atmosphere inside an MBraun drybox using a CH Instrument CHI630D Potentiostat in a single compartment cell using 1 mM sample solutions in acetonitrile with 0.1 M tetrabutylammonium hexafluorophosphate as supporting electrolyte. A three-electrode setup was employed with a glassy carbon electrode as working electrode, a platinum sheet as the counter electrode and a silver wire as a quasi-reference electrode. Ferrocene was added as an internal standard after completion of the measurements, and all potentials are referenced versus the $Fc^{+/0}$ couple. Solution and solid IR spectra were recorded on a PerkinElmer Spectrum 100 FT-IR spectrometer.

Preparation of $K[Fe(CN)(CO)_4]$. Method 1: In a drybox, a solution of $Fe(CO)_5$ (4.6 g, 23.48 mmol, 1.0 equiv) in 10 mL of pentane was added dropwise to a 100-mL round bottom flask containing a solution of $K[N(SiMe_3)_2]$ (4.92 g, 24.66 mmol, 1.05 equiv) in 60

mL of Et_2O/pentane (1:10) mixture. **This reaction is exothermic, and the solvent quickly boils if $Fe(CO)_5$ is added too fast.* The off-white precipitate appeared rapidly. After stirring at room temperature for 2 h, the suspension was filtered. The desired product in the precipitate was extracted into 30 mL of Et_2O. The extracts were concentrated to 15 mL. Addition of 50 mL of pentane precipitated $K[Fe(CN)(CO)_4]$ as a white solid. Yield: 4.39 g (80%). IR (MeCN, ν/cm^{-1}) 2109 (w), 2038 (s), 1949 (s), 1929 (vs). ^{13}C NMR (151 MHz, CD_3CN, δ): 217.63, 139.16. Anal. Calcd for C_5FeKNO_4: C, 25.77; H, 0.00, N, 6.01 Found: C, 25.71; H, 0.04; N, 5.87. **Method 2:** In a drybox, $Fe_3(CO)_{12}$ (148 mg, 0.294 mmol, 1.0 equiv) and KCN (77.0 mg, 1.18 mmol, 4.00 equiv) were loaded in a 20-mL vial followed by 10 mL of MeOH. After stirring at 50 ºC for 1 h, the initial dark green suspension turned to a light orange solution (slightly cloudy). Solvent was removed under vacuum. The product was extracted into Et_2O (30 mL). The combined extracts were concentrated to 4 mL. Layering of the concentrate with 8 mL of pentane gave crystals of $K[Fe(CN)(CO)_4]$ upon standing at RT. Yield: 140 mg (68%).

Preparation of $K[Fe(^{13}CN)(CO)_4]$. In a drybox, $Fe_3(CO)_{12}$ (1 g, 1.99 mmol, 1.0 equiv) and $K^{13}CN$ (406 mg, 6.16 mmol, 3.10 equiv) were loaded in a 20-mL vial followed by 15 mL of MeOH. After stirring at 60 ºC for 2 h, the initially dark green suspension turned to a cloudy orange-brown or purple-red solution. The solvent was removed under vacuum. The desired product was extracted into Et_2O. The combined extracts were concentrated to 4 mL. About 8 mL of pentane was layered on the top of the Et_2O solution. $K[Fe(^{13}CN)(CO)_4]$ crystals appeared upon standing at RT. The resulting dark red crystalline solid was collected. **The color in the product resulted from trace amount of highly colored impurities, which have no effect on later steps*. Yield: 778 mg (56%). IR (MeCN, ν/cm^{-1}) 2033 (s, CO), 1948 (s, CO), 1929 (vs, CO). *CN band was not found, presumably overlapped with one of CO bands. ^{13}C NMR (151 MHz, CD_3CN, δ): 217.63 (d, J = 9.4 Hz), 139.11. Anal. Calcd for $C_4{}^{13}CFeKNO_4$: C, 25.77; H, 0.00, N, 6.01 Found: C, 25.63; H, 0.08; N, 5.84. Single crystals suitable for X-ray crystallographic analysis were grown by layering a Et_2O solution of $K[Fe(^{13}CN)(CO)_4]$ with pentane at RT.

Preparation of $[K_2(18\text{-crown-}6)_2(thf)][Fe_2(\mu\text{-}SH)_2(CN)_2(CO)_4]$. In a drybox, $K[Fe(CN)(CO)_4]$ (500 mg, 2.15 mmol, 1.0 equiv) was dissolved in 30 mL of Et_2O in a 100-mL round bottomed flask. The flask was then charged with 30 mL of pentane and 4 g of

ground glass pieces *(*to prevent the photodegraded products depositing on the surface of the reaction flask, which inhibits light penetration)*. The reaction mixture was continuously purged with H_2S gas (~2 bubbles/s) while irradiating with 365 nm light. **The amount of solvent decreases over time due to slow evaporation.* The reaction flask was cooled with a stream of air to minimize solvent evaporation. A dark orange solid precipitated appeared over the course of 2 h. The reaction mixture was then purged with N_2 to remove excess H_2S and returned to the drybox. The suspension was filtered, and the precipitate was washed with Et_2O (3 x 5 mL). The combined filtrates were subjected to further treatment with H_2S/UV. The suspension was again filtered (using the same filter from the first run), and the combined precipitates were washed with Et_2O (3 x 5 mL). The desired product in the precipitate was extracted into THF (4 x 5 mL). The combined extracts were concentrated to 3 mL. To the concentrated THF solution was added 5 mL of Et_2O. After standing at RT for 1 d, the THF/Et_2O mixture was filtered to remove black solids. Solvent was removed from the filtrate to give about 180 mg of dark orange oil. **This oil is assumed to be 100% "$K_2[Fe_2(\mu\text{-}SH)_2(CN)_2(CO)_4]$" for calculating the amount of 18-crown-6 needed*. To the crude oil was added 18-crown-6 (226 mg, 0.857 mmol) followed by 1.5 mL of MeCN and 2.5 mL of THF. The homogeneous dark orange-brown MeCN/THF solution was layered with 5 mL of Et_2O. After standing at RT for 1 day, the Et_2O-MeCN/THF solution deposited dark red-orange crystals of $[K_2(18\text{-crown-}6)_2(thf)][Fe_2(\mu\text{-}SH)_2(CN)_2(CO)_4]$. Solvents were decanted, and the $[K_2(18\text{-crown-}6)_2(thf)][Fe_2(\mu\text{-}SH)_2(CN)_2(CO)_4]$ crystals were washed with THF (3 x 2 mL) and Et_2O (1 x 2 mL). After drying under vacuum, the $[K_2(18\text{-crown-}6)_2(thf)][Fe_2(\mu\text{-}SH)_2(CN)_2(CO)_4]$ was collected as dark wine or dark orange crystals. Yield: 86 mg (8%). **This yield is typical for the repeated or slightly modified batches.* IR (MeCN, ν/cm^{-1}) 2080 (m, CN), 1971 (s, CO), 1931 (s, CO), 1893 (s, CO), ~1883 (m, CO, a shoulder peak). IR (solid, ν/cm^{-1}) 2501 (w, SH). ^{1}H NMR (600 MHz, CD_3CN, δ): 3.67 – 3.63 (m, CH_2O from THF), 3.57 (s, CH_2O from 18-crown-6), 1.84 – 1.76 (m, CH_2 from THF), -1.13 (s, **e**-H of the **ae** isomer), -1.78 (s, **e**-H of the **ee** isomer), -3.91 (s, **a**-H of the **ae** isomer), -3.96 (s, **a**-H of the **aa** isomer). **The ^{1}H resonances are assigned based on the analysis of reported similar compound, $Fe_2(\mu\text{-}SH)_2(CO)_4(PPh_3)_2$.* [1] *The assignment is further supported by DFT calculation (vide infra).* ^{13}C NMR (151 MHz, CD_3CN, δ): 222.04 (*C*O from **ae** isomer), 221.43 (*C*O from **ae**

isomer), 221.24 (*C*O from **aa** isomer), 148.85 (*C*N from **ae** isomer), 148.13 (*C*N from **aa** isomer), 70.90 (*C* from 18-crown-6), 68.26 (*C*H_2O from THF), 26.22 (*C*$H_2$$CH_2$ from THF), **^{13}C signals for CO and CN of **ee** isomer is not observed even on a concentrated sample.* Anal. Calcd for $C_{34}H_{58}Fe_2K_2N_2O_{17}S_2$: C, 40.00; H, 5.73; N, 2.74; Found: C, 40.09; H, 5.42; N, 3.11. Single crystals suitable for X-ray crystallographic analysis were grown by layering a MeCN/THF solution of $[K_2(18\text{-crown-6})_2(thf)][Fe_2(\mu\text{-}SH)_2(CN)_2(CO)_4]$ with Et_2O at RT for 1 d.

Preparation of $[K_2(18\text{-crown-6})_2(thf)][Fe_2(\mu\text{-}SH)_2(^{13}CN)_2(CO)_4]$. This compound was prepared from $K[Fe(^{13}CN)(CO)_4]$ using the same method for $[K_2(18\text{-crown-6})_2(thf)][Fe_2(\mu\text{-}SH)_2(^{12}CN)_2(CO)_4]$. Using 262 mg of $K[Fe(^{13}CN)(CO)_4]$, the reaction gave 67 mg (12% yield) of the desired product. IR (MeCN, ν/cm^{-1}): 2035 (m, ^{13}CN), 1970 (s, CO), 1930 (s, CO), 1893 (s, CO), ~1882 (m, CO, a shoulder peak). ^{1}H NMR (600 MHz, CD_3CN, δ): 3.66 – 3.61 (m, CH_2O from THF), 3.57 (s, CH_2O from 18-crown-6), 1.83 – 1.75 (m, CH_2 from THF), -1.13 (s, **e**-H of the **ae** isomer), -1.79 (s, **e**-H of the **ee** isomer), -3.92 (s, **a**-H of the **ae** isomer), -3.96 (s, **a**-H of the **aa** isomer). ^{13}C NMR (151 MHz, CD_3CN, δ): 222.06 (*C*O from **ae** isomer), 221.44 (*C*O from **ae** isomer), 221.25 (*C*O from **aa** isomer), 149.61(*C*N from **ee** isomer), 148.85 (*C*N from **ae** isomer), 148.09 (*C*N from **aa** isomer), 70.90 (*C* from 18-crown-6), 68.26 (*C*H_2O from THF), 26.23 (*C*$H_2$$CH_2$O from THF). Anal. Calcd for $C_{32}{}^{13}C_2H_{58}Fe_2K_2N_2O_{17}S_2$: C, 40.00; H, 5.73; N, 2.74; Found: C, 39.78; H, 5.43; N, 3.41.

HydG/HydE-less *in vitro* maturation of *Cr*HydA1. The experiments were performed according to the procedure described in references [2-3] with minor modifications, which requires clear *E. coli* cell lysates containing untagged *So*HydF (*Shewanella oneidensis*) enzyme as well as apo-*Cr*HydA1 (*Chlamydomonas reinhardtii*) enzyme with an N-terminal *strep*-tag II, compound [**2**] and small molecules GTP and PLP. Therefore, the HydG/HydE-less *in vitro* maturation medium in this work contains:

(1) *E. coli* cell lysate;
(2) HydF enzyme;
(3) apo-HydA1 enzyme;
(4) synthetic diiron complex [**2**]$^{2-}$;
(5) GTP and PLP.

To make cell lysate containing untagged *So*HydF (~10 μM) or strep-tagged apo-*Cr*HydA1 (~10 μM), recombinant *E. coli* cells containing the corresponding plasmid were grown, induced and lysed. Clear cell lysate was aliquoted (~5 mL) and stored at −80 °C for further use.

For the maturation of *Cr*HydA1, a reaction mixture (~10 mL) was prepared, including 5 mL apo-*Cr*HydA1 lysate, 5 mL *So*HydF lysate, 1 mM pyridoxal phosphate (PLP), 20 mM guanosine triphosphate (GTP), and ~4 mg complex [**2**] (added in order). The pH of the reaction mixture was adjusted to ~7.5. The reaction mixture was incubated at room temperature in an anaerobic chamber containing 4% H_2 for ~2 h and then clarified by centrifugation. The maturated *Cr*HydA1 was purified and isolated from the supernatant by using ~5 mL *strep*-tactin resin. Fraction containing *Cr*HydA1 protein was collected, concentrated and flash frozen in liquid nitrogen and stored at −80 °C. To make the EPR sample, 2 mM thionine was added to ~500 μM *Cr*HydA1. The mixture was immediately transferred into the EPR tube and flash frozen in liquid nitrogen for further EPR spectroscopic analysis (Fig. 4). Control experiments by omitting HydF as shown Fig. 1B and Fig. S13 were conducted by omitting the *So*HydF enzyme from the above HydG/HydE-less maturation mixture.

In order to confirm that the bridging $HN(CH_2)_2$ group was installed on the $Fe_2(SH)_2$ core of $[\mathbf{2}]^{2-}$, we added 3-^{13}C/^{15}N-labeled serine (~2 mM) in the maturation medium. Note that our previous work[10] had identified 3-C and N of serine as the source of the respective C and N centers of the bridging $HN(CH_2)_2$ group. In terms of the serine chemistry, two possible PLP-dependent enzymes in *E. coli* common metabolic pathways have been hypothesized[10] to be in charge of serine transformations: serine dehydratase and serine hydroxymethyltransferase. Serine dehydratase uses the PLP cofactor to catalyze the deamination of serine to yield ammonia and pyruvate.[4] Serine hydroxymethyltransferase is also a PLP-dependent enzyme that plays an important role in serving one carbon unit C1 to the cell by transferring the 3-C methylene group of serine.[5]

EPR spectroscopy and analysis. X-band (9.37 GHz) CW EPR spectra (Fig. 4A&4E and Fig. S13) were recorded on a Bruker (Billerica, MA) EleXsys E500 spectrometer equipped with a super-high Q resonator (ER4122SHQE). Cryogenic

temperatures were achieved and controlled using an ESR900 liquid helium cryostat in conjunction with a temperature controller (Oxford Instruments ITC503) and a gas flow controller. CW EPR spectra were recorded at 15 K by using 0.02 mW power under slow-passage conditions. The spectrometer settings were as follows: conversion time of 40 ms, modulation amplitude of 0.5 mT and modulation frequency of 100 kHz. Other settings are given in the corresponding figure captions. Simulations of the CW spectra and the following pulse EPR spectra were performed using EasySpin 5.1.10 toolbox[6-7] within the Matlab 2014a software suite (The Mathworks Inc., Natick, MA).

Q-band (~34.0 GHz) pulse ENDOR experiments were performed on a Bruker Biospin EleXsys 580 spectrometer equipped with a 10 W amplifier and a R.A. Isaacson cylindrical TE_{011} resonator in an Oxford CF935 cryostat. ENDOR measurements were performed at 15 K by employing the Mims pulse sequence (π/2-τ-π/2-RF-π/2-τ-echo) for small hyperfine couplings[8] or Davies pulse sequence (π-RF-π/2-τ-π-τ-echo) for larger hyperfine couplings.[9] ENDOR spectra were collected stochastically by randomly hopping the RF excitation frequency.[10] Pulse sequences were programmed with the PulseSPEL programmer via the Xepr interface.

For a single molecular orientation with respect to the applied magnetic field, a nucleus (N) with nuclear spin of I = 1/2 (e.g., ^{13}C and ^{15}N in this work) that is hyperfine coupled to an S = 1/2 electron spin will give rise to two ENDOR transitions appearing at positions that are a function of ν_N, the nuclear Larmor frequency, and A, the orientation-dependent hyperfine interaction (HFI) tensor.[11] If the HFI is weak (when $\nu_N > A/2$), the observed ENDOR transitions are centered at the ν_N of the nucleus and split by the HFI A, which applies to the cases of ^{13}C-ENDOR (Fig. 4B&4F) and ^{15}N-ENDOR (Fig. 4C) in this work.

For Mims-ENDOR experiments,[8] the ENDOR intensities are modulated by the response factor (R) which is a function of the hyperfine coupling A and the time interval (τ) between the first and the second π/2 microwave pulse in the three-pulse sequence: $R \sim [1-\cos(2\pi A\tau)]$. When $A\tau$ = n (n = 0, 1, 2, 3 ...), this factor will be zero, corresponding to a minima in the ENDOR response, i.e., the hyperfine “suppression holes” in Mims-ENDOR spectra. This Mims-hole effect can be avoided by adjusting the τ value. For this

reason varying τ values of 260 ns and 300 ns were used for ^{13}C Mims-ENDOR experiments at g_1 2.103 and g_3 1.998, respectively (Fig. 4B), and 260 ns was used for ^{15}N Mims-ENDOR experiments at both g_1 2.103 and g_3 1.998 (Fig. 4C).

The ^{13}C and ^{15}N hyperfine coupling interactions for the bridging $^{15}NH(^{13}CH_2)_2$ at H_{ox} state were obtained by simulating the ^{13}C and ^{15}N Mims-ENDOR spectra shown in Fig. 4B&4C using the parameters of **g** = [2.103, 2.041, 1.998]; $A(^{13}C1)$ = [3.40, 1.35, 1.37] MHz, Euler angle = [21, 21, 0]°; $A(^{13}C2)$ = [0.28, 1.32, 1.38] MHz, Euler angle = [25, 6, 0]°; $A(^{15}N)$ = [1.90, 1.57, 1.63] MHz, Euler angle = [0, 0, 0]°. The hyperfine interactions are identical to previously reported values.[12] The ^{13}C hyperfine coupling interactions for the two CN^- ligands at H_{ox} state were obtained by simulating the ^{13}C Davies-ENDOR spectra shown in Fig. 4F using the parameters of **g** = [2.103, 2.041, 1.998]; $A(^{13}C_{distal})$ = [30.2, 26.2, 29.0] MHz, Euler angle = [70, 50, 70]°; $A(^{13}C_{proximal})$ = [5.26, 5.24, 4.46] MHz, Euler angle = [30, 0, 0]°, similar as previously reported values.[13]

H_2 production assay. H_2 production assay were performed according to previous procedures.[3, 14] Briefly, the reaction mixture (a total volume of 3 mL) at 20 °C was prepared in a 15 mL sealed tube under N_2 atmosphere, containing 0.1 μM maturated HydA1 and 5 mM methyl viologen in pH = 6.8 phosphate buffer. The reaction was initiated by injecting 30 μL 1 M freshly made sodium dithionite and was continued for ~30 min. H_2 production was monitored by injecting 500 μL headspace every 5 min into a Varian 3800 gas chromatography equipped with a 60/80 Å molecular sieve and the thermal conductivity detector.

NMR spectrum

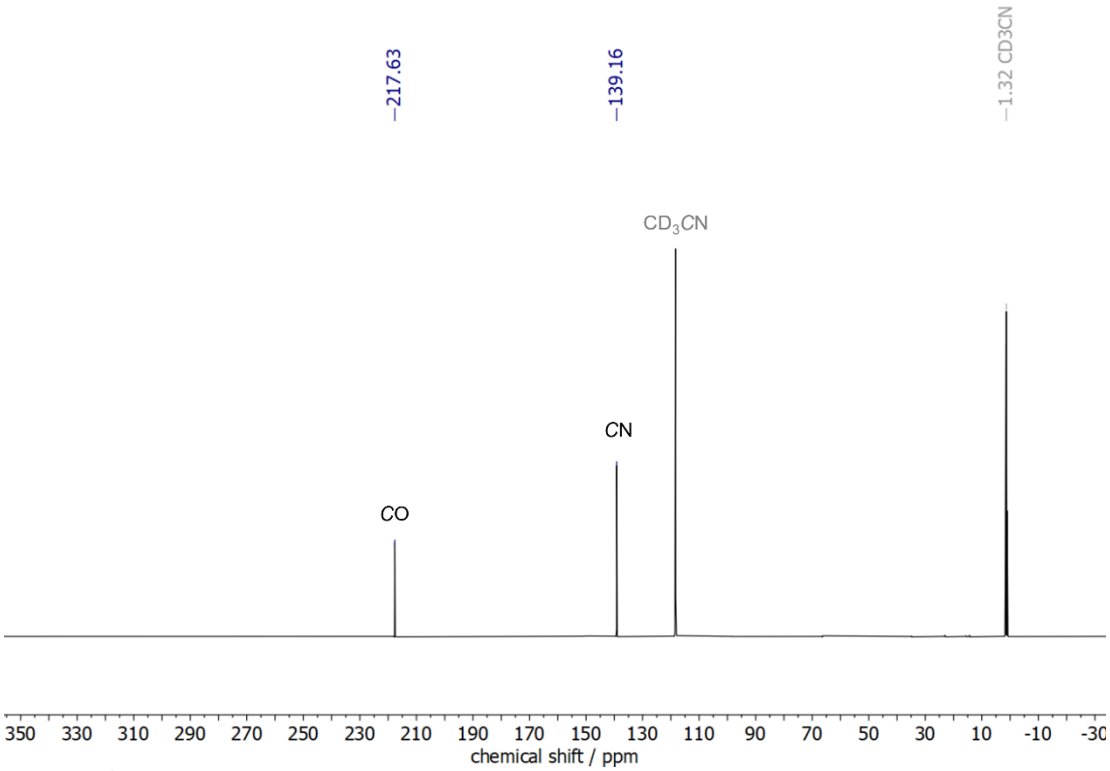

Figure S1. ^{13}C NMR spectrum of $K[Fe(CN)(CO)_4]$ in CD_3CN solution under N_2.

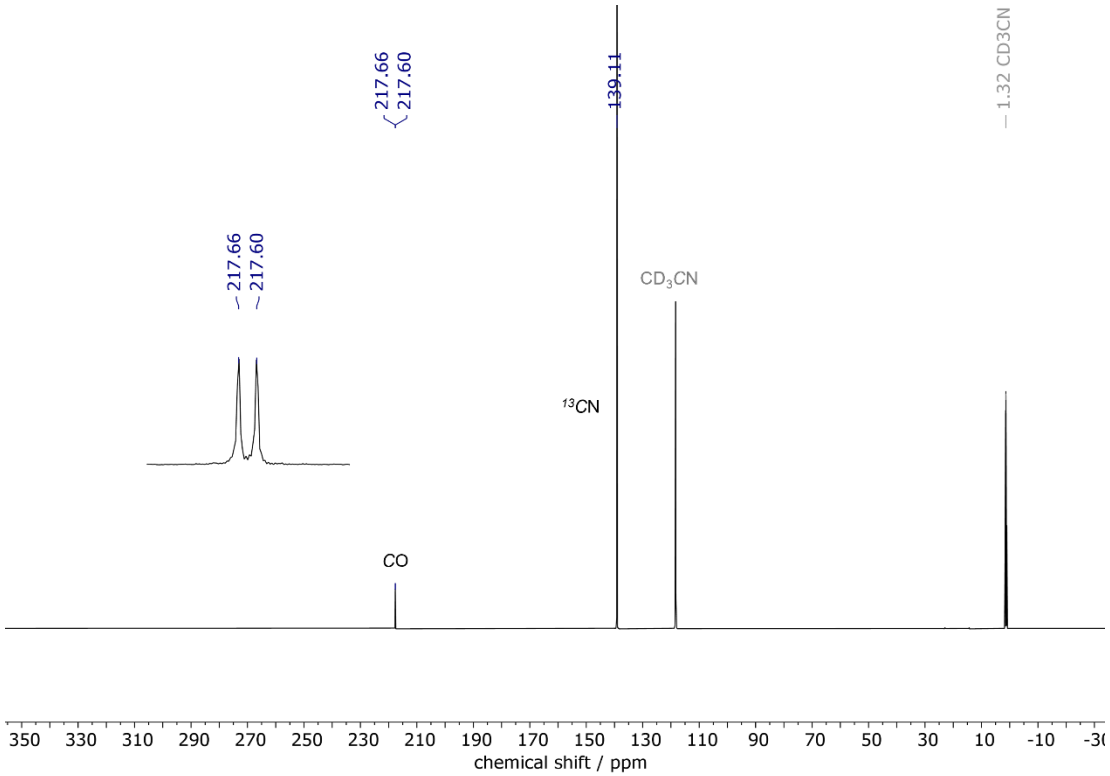

Figure S2. ^{13}C NMR spectrum of $K[Fe(^{13}CN)(CO)_4]$ in CD_3CN solution under N_2.

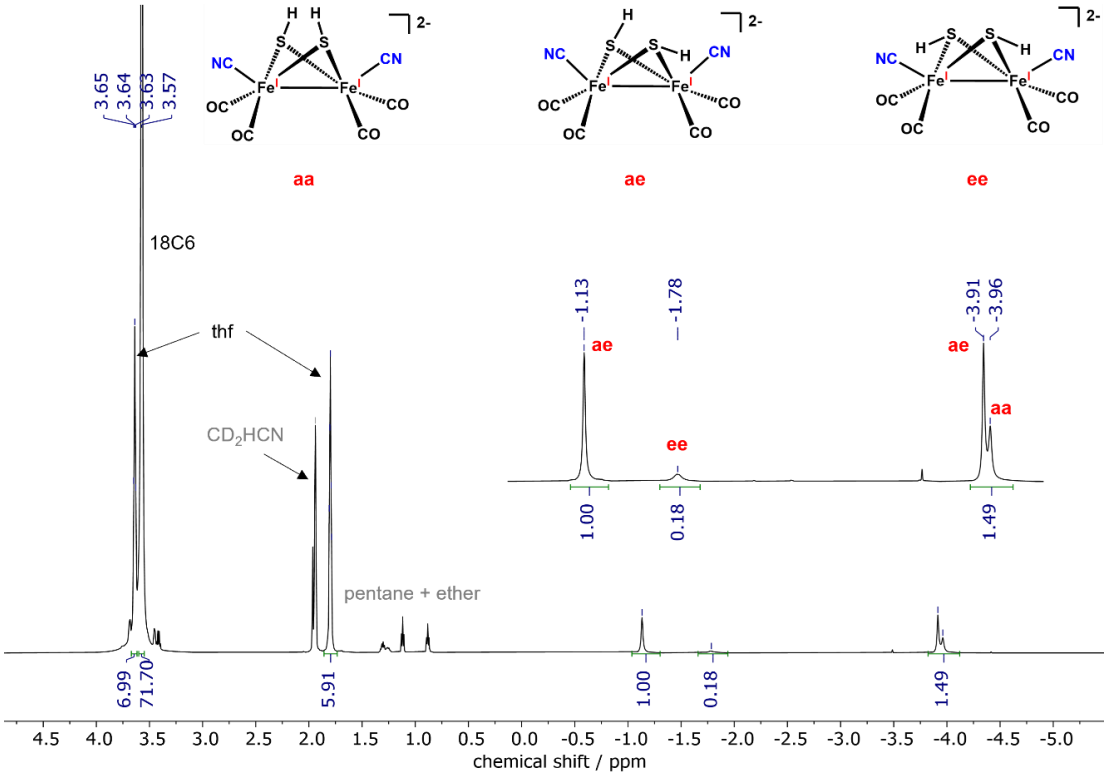

Figure S3. ^{1}H NMR spectrum of $[K_2(18\text{-crown-}6)_2(thf)][Fe_2(\mu\text{-}SH)_2(CN)_2(CO)_4]$ in CD_3CN solution under N_2.

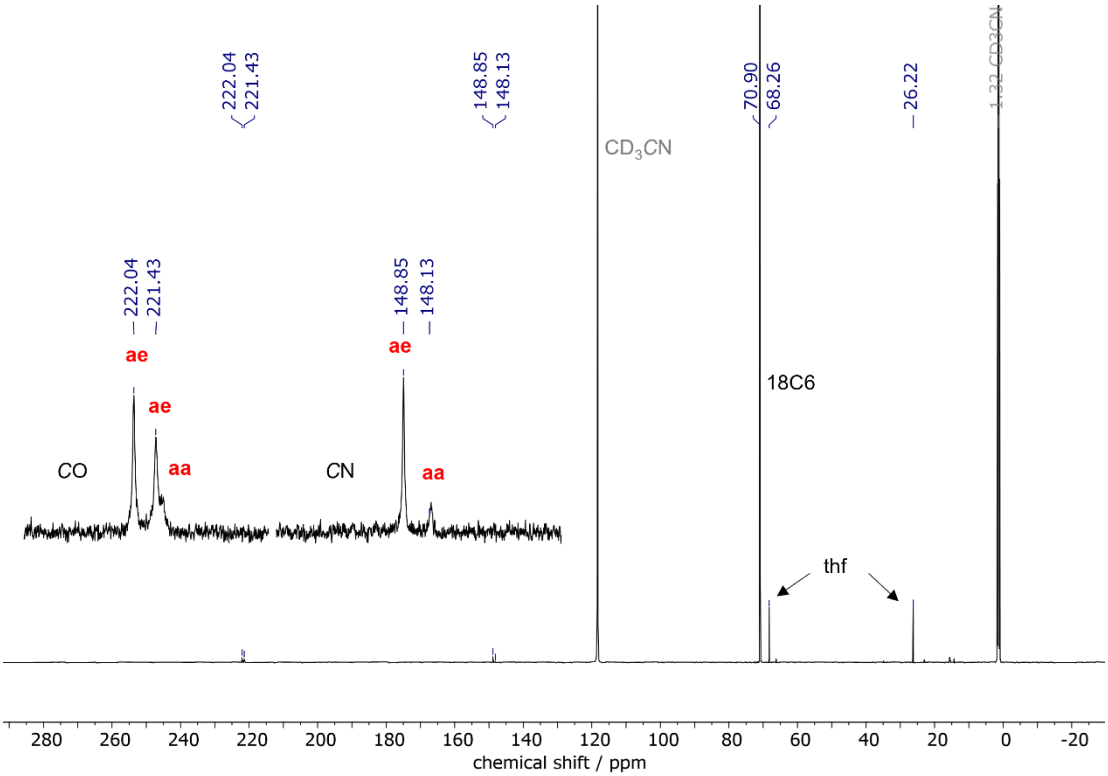

Figure S4. ^{13}C NMR spectrum of $[K_2(18\text{-crown-}6)_2(thf)][Fe_2(\mu\text{-}SH)_2(CN)_2(CO)_4]$ in CD_3CN solution under N_2.

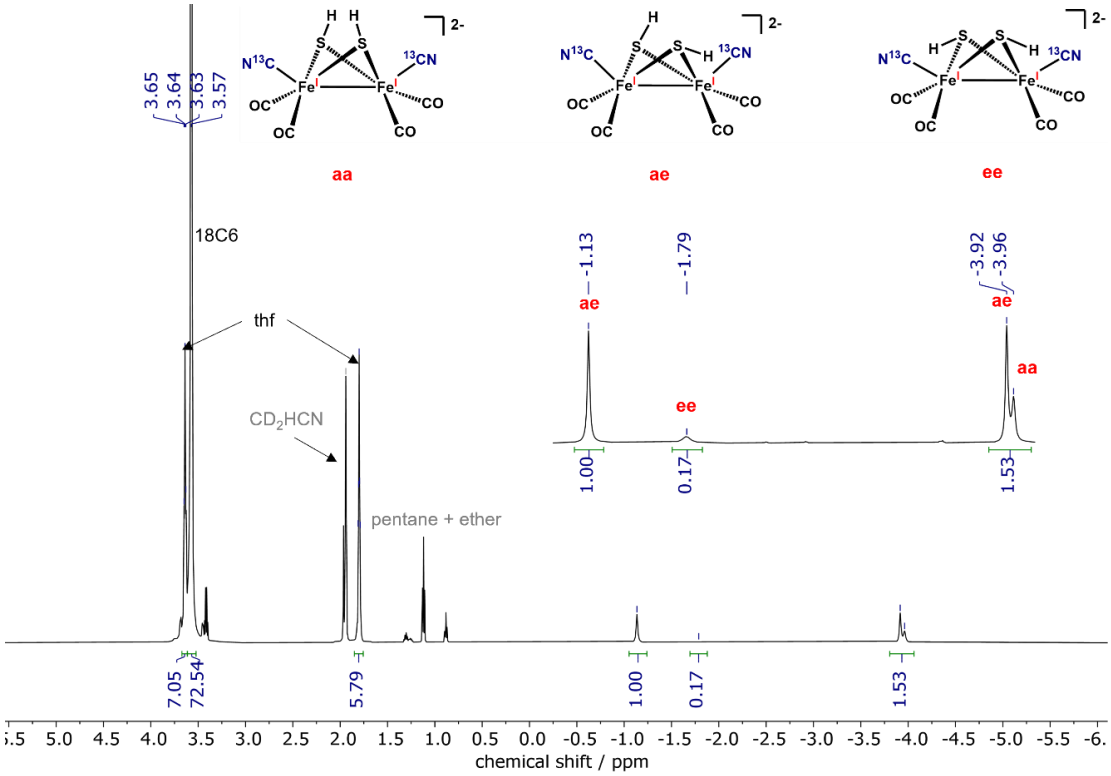

Figure S5. ^{1}H NMR spectrum of $[K_2(18\text{-crown-}6)_2(thf)][Fe_2(\mu\text{-}SH)_2(^{13}CN)_2(CO)_4]$ in CD_3CN solution under N_2.

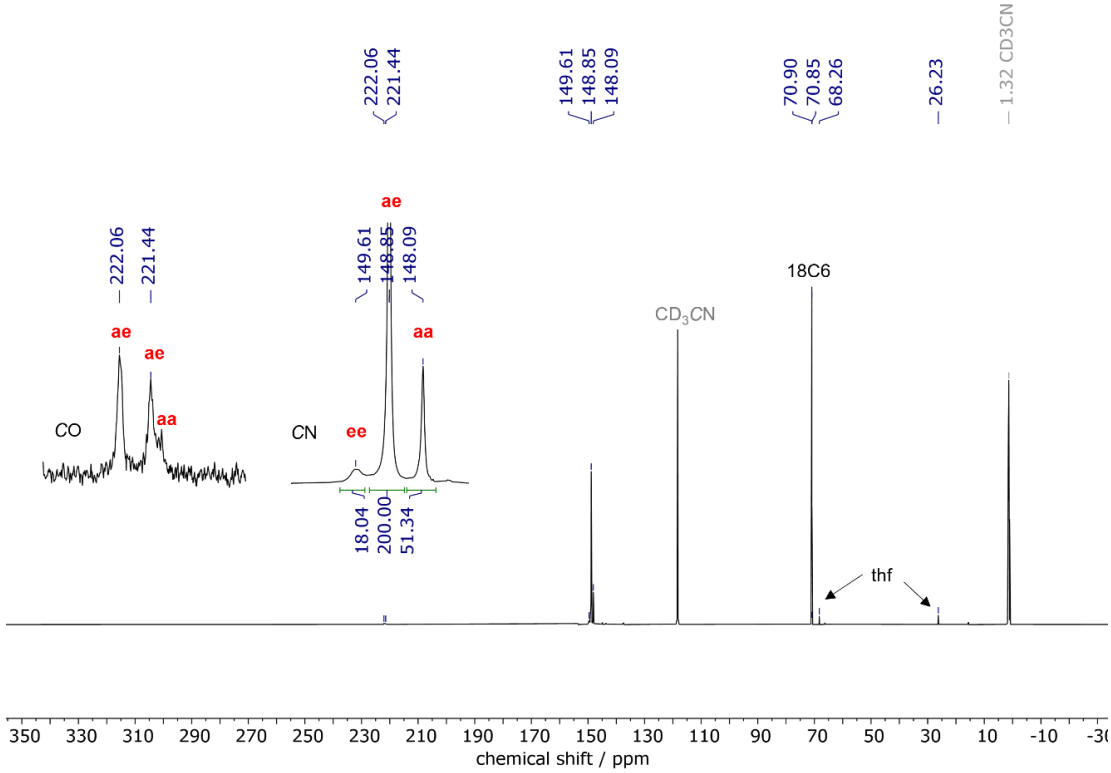

Figure S6. ^{13}C NMR spectrum of $[K_2(18\text{-crown-}6)_2(thf)][Fe_2(\mu\text{-}SH)_2(^{13}CN)_2(CO)_4]$ in CD_3CN solution under N_2.

X-ray Crystallography

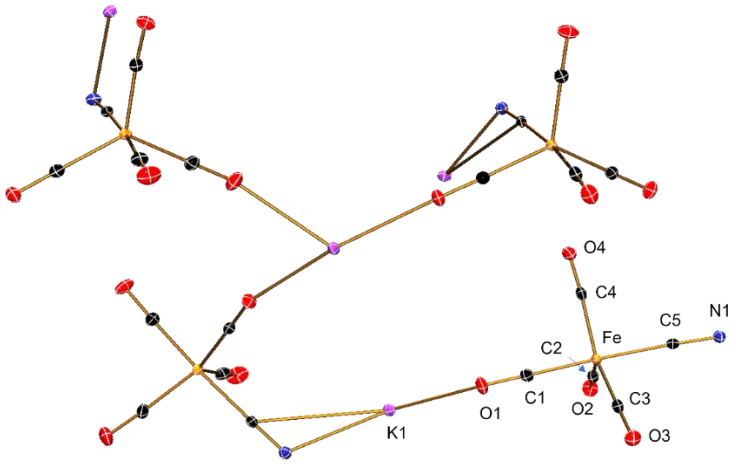

Figure S7. The crystal structure of $\{K[Fe(^{13}CN)(CO)_4]\}_n$.

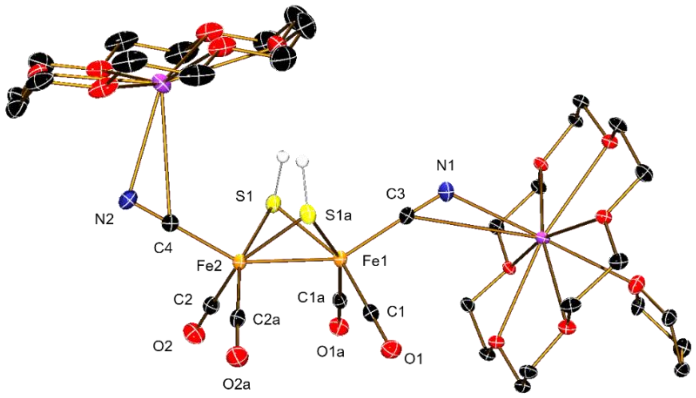

Figure S8. The crystal structure of $[K_2(18\text{-crown-6})_2(thf)][Fe_2(\mu\text{-}SH)_2(CN)_2(CO)_4]$.

Table S1. Selected bond distances (Å) for $[K_2(18\text{-crown-6})_2(thf)][Fe_2(\mu\text{-}SH)_2(CN)_2(CO)_4]$.

Fe(1)-C(1)a	1.751(3)
Fe(1)-C(1)	1.751(3)
Fe(1)-C(3)	1.945(4)
Fe(1)-S(1)	2.2960(8)
Fe(1)-S(1)a	2.2960(8)
Fe(1)-Fe(2)	2.4952(7)
Fe(2)-C(2)	1.751(3)
Fe(2)-C(2)a	1.751(3)
Fe(2)-C(4)	1.944(4)
Fe(2)-S(1)	2.3006(8)
Fe(2)-S(1)a	2.3006(8)

Table S2. Crystallographic Data Collection and Refinement Details.

	$K[Fe(^{13}CN)(CO)_4]$	$[K_2(18\text{-crown-6})_2(thf)][Fe_2(\mu\text{-}SH)_2(CN)_2(CO)_4]$
Identification code	ed73Ls	ed07Ls
Empirical formula	C_5 Fe K N O_4	C_{34} H_{56} Fe_2 K_2 N_2 O_{17} S_2
Formula weight	233.01	1018.82
Temperature	120(2) K	100(2) K
Wavelength	0.71073 Å	0.71073 Å
Crystal system	Monoclinic	Monoclinic
Space group	I2/a	$P2_1/m$
Unit cell dimensions	a = 17.7970(5) Å	a = 9.8893(2) Å
	b = 10.2186(3) Å	b = 14.0021(2) Å
	c = 35.6036(11) Å	c = 17.2225(3) Å
Volume	6445.9(3) $Å^3$	2363.61(7) $Å^3$
Z	32	2
Density (calculated)	1.921 Mg/m^3	1.432 Mg/m^3
Absorption coefficient	2.357 mm^{-1}	0.944 mm^{-1}
F(000)	3648	1064
Crystal size	0.598 x 0.474 x 0.304 mm^3	0.282 x 0.266 x 0.026 mm^3
Theta range for data collection	1.979 to 28.291°.	2.254 to 28.294°.
Index ranges	-23 ≤ h ≤ 23, -13≤ k ≤ 13, -47 ≤l ≤ 47	-13 ≤ h ≤ 13, -18 ≤ k ≤ 18, -22 ≤ l ≤ 22
Reflections collected	95958	85129
Independent reflections	8019 [R(int) = 0.0362]	6106 [R(int) = 0.0347]
Completeness to theta = 25.242°	100.0 %	99.9 %
Absorption correction	Semi-empirical from equivalents	Semi-empirical from equivalents
Max. and min. transmission	0.7457 and 0.4919	0.7457 and 0.6835
Refinement method	Full-matrix least-squares on F^2	Full-matrix least-squares on F^2
Data / restraints / parameters	8019 / 0 / 434	6106 / 706 / 494
Goodness-of-fit on F^2	1.064	1.081
Final R indices [I>2sigma(I)]	R1 = 0.0233, wR2 = 0.0707	R1 = 0.0460, wR2 = 0.1213
R indices (all data)	R1 = 0.0239, wR2 = 0.0712	R1 = 0.0492, wR2 = 0.1233
Extinction coefficient	n/a	n/a
Largest diff. peak and hole	0.506 and -0.557 $e.Å^{-3}$	1.078 and -1.210 $e.Å^{-3}$

Additional IR spectra

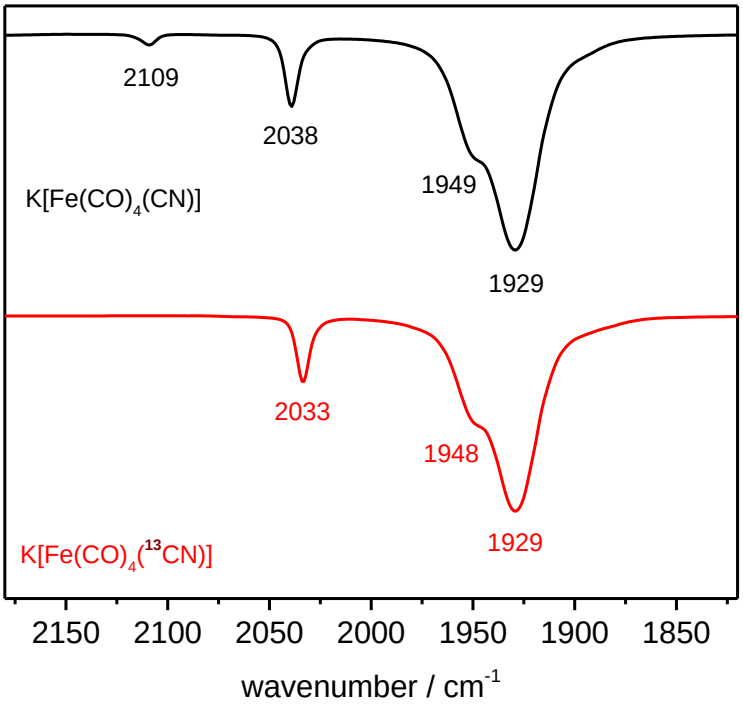

Figure S9. FT-IR spectra of $K[Fe(CN)(CO)_4]$ (black) and $K[Fe(^{13}CN)(CO)_4]$ (red) in CH_3CN solution under N_2.

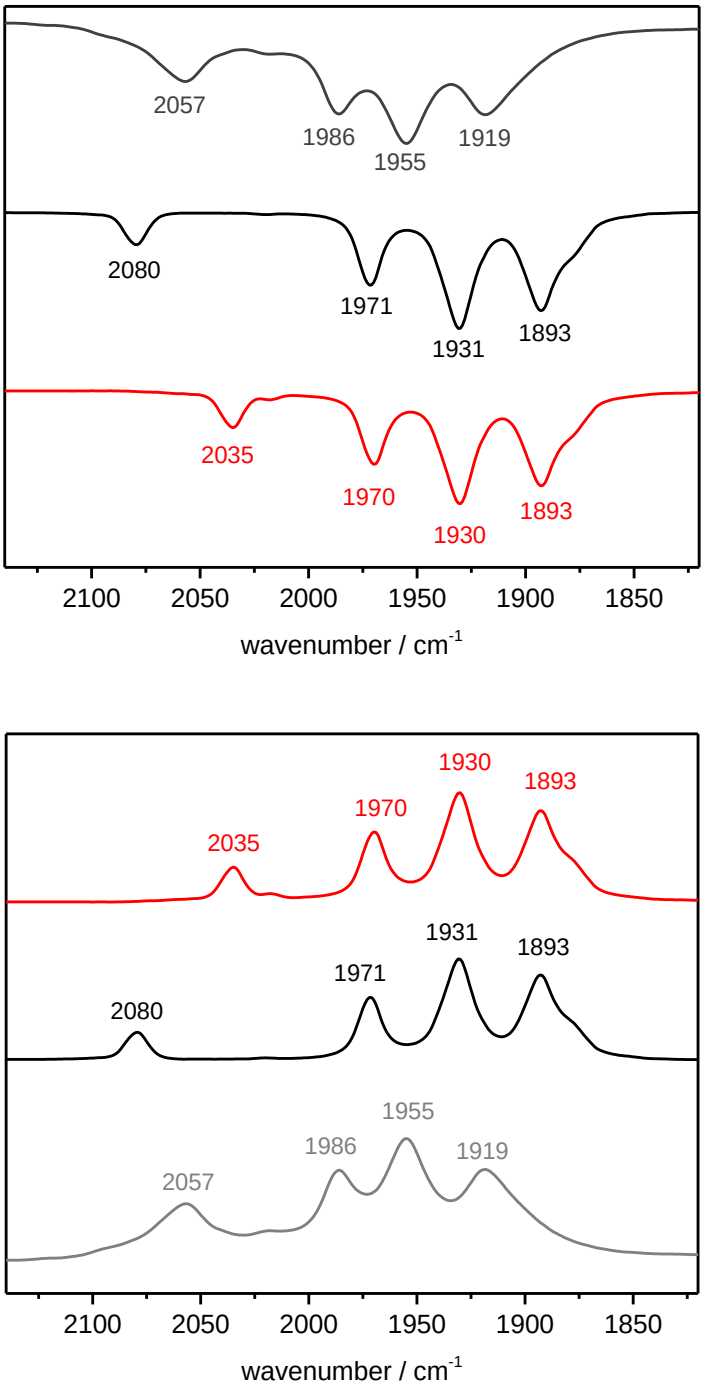

Figure S10. FT-IR spectra of $[K_2(18\text{-crown-6})_2(thf)][Fe_2(\mu\text{-}SH)_2(CN)_2(CO)_4]$ (dark gray: in D_2O; black: in CH_3CN) and $[K_2(18\text{-crown-6})_2(thf)][Fe_2(\mu\text{-}SH)_2(^{13}CN)_2(CO)_4]$ (red) in CH_3CN solution under N_2. Top: Transmittance mode; bottom: absorbance mode.

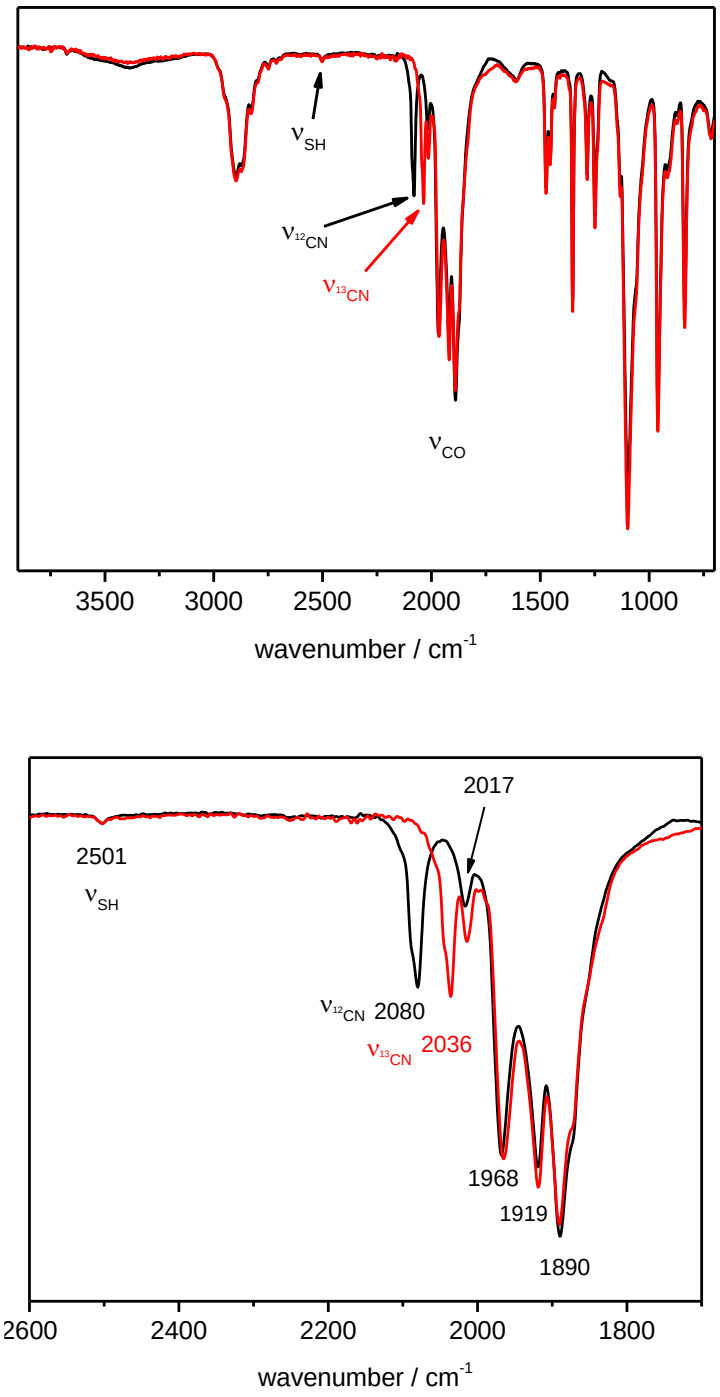

Figure S11. FT-IR spectra of $[K_2(18\text{-crown-6})_2(thf)][Fe_2(\mu\text{-}SH)_2(CN)_2(CO)_4]$ (black) and $[K_2(18\text{-crown-6})_2(thf)][Fe_2(\mu\text{-}SH)_2(^{13}CN)_2(CO)_4]$ (red) as a solid. Top: The full spectrum. Bottom: a zoomed-in region for SH, CN, and CO bands.

Additional EPR spectrum

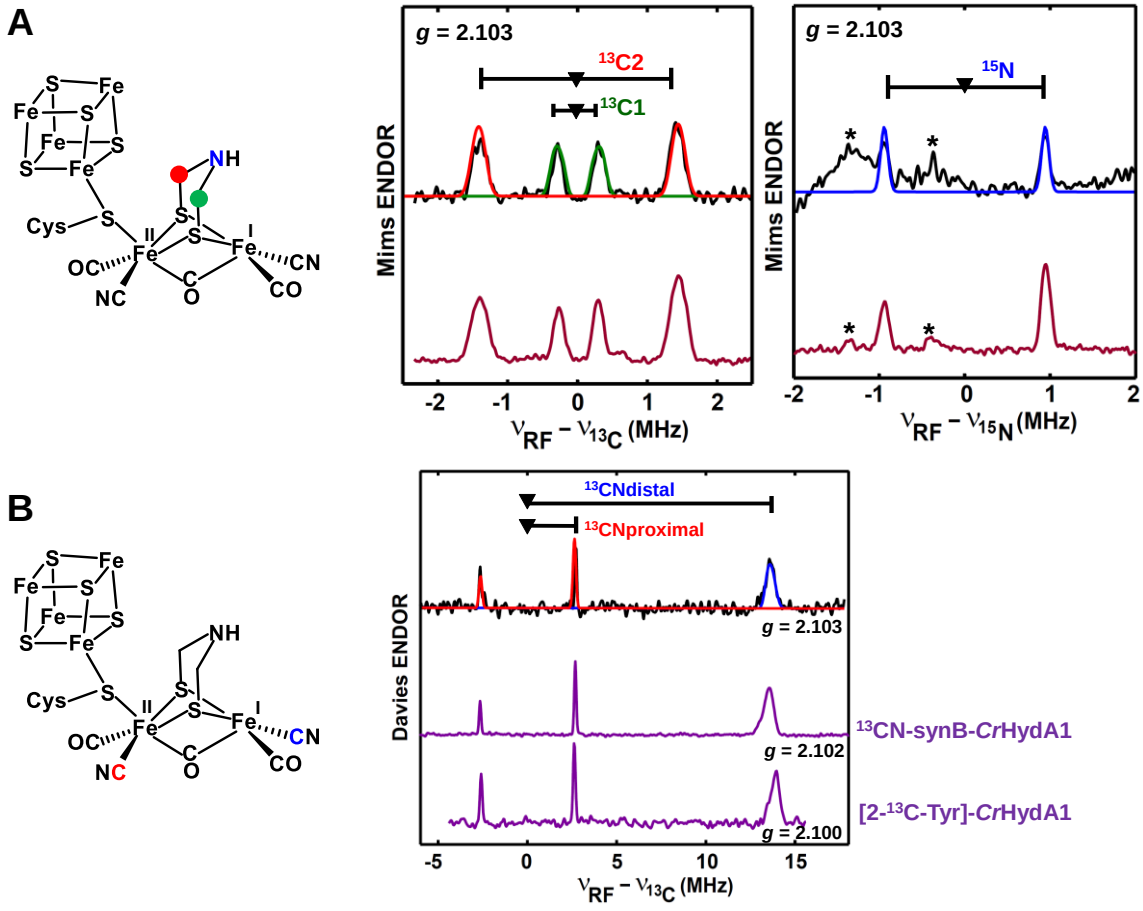

Figure S12. **(A)** Q-band ^{13}C- and ^{15}N-Mims ENDOR spectra of [**2**]$^{2-}$-*Cr*HydA1 with the isotope-labeled ^{15}NH(^{13}CH$_2$)$_2$ bridgehead (*see* Fig. 4B&C), recorded at g_1 2.103 of H$_{ox}$. The burgundy spectra are the corresponding ^{13}C- and ^{15}N-Mims ENDOR spectra of H$_{ox}$ sample obtained by *in vitro* maturation using HydG, HydE, HydF lysate as well as ^{13}C/^{15}N-labeled serine, adapted from reference.[12] **(B)** Q-band ^{13}C-Davies ENDOR spectra of the ^{13}CN-[**2**]$^{2-}$-*Cr*HydA1 (*see* Fig. 4F), recorded at g_1 2.103 of H$_{ox}$. The purple spectra are the corresponding ^{13}C-Davies ENDOR spectra of H$_{ox}$ samples obtained by *in vitro* maturation using HydG, HydE, HydF lysate as well as 2-^{13}C-tyrosine, or by HydG-less maturation using ^{13}CN-labeled syn-B compound, adapted from reference.[12]

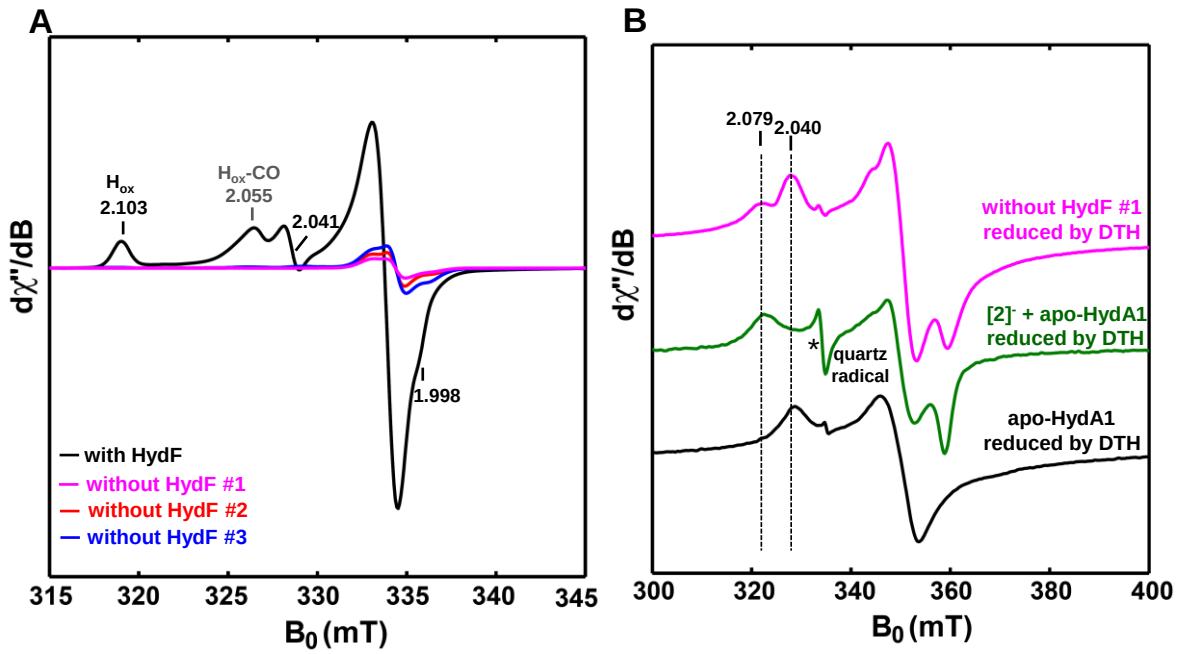

Figure S13. (**A**) X-band CW EPR spectra (15 K) of the maturated *Cr*HydA1 oxidized by thionine. The black trace, also shown in Fig. 4A, is the *Cr*HydA1 from HydG/HydE-less maturation by using [**2**]$^{-}$. The spectra in magenta, red and blue are the maturated *Cr*HydA1 (oxidized by thionine) obtained by omitting HydF from HydG/HydE-less maturation. This control experiment was repeated for three times as indicated by the number #. Neither H_{ox} nor H_{ox}-CO EPR signal was observed, suggesting that no H-cluster was assembled. The signal at ~ g 2.0 with low signal intensity arises from the thionine-related radical species. (**B**) The magenta trace is the no-HydF maturated *Cr*HydA1 sample reduced by dithionite (DTH), suggesting the final HydA1 contains both apo-HydA1 and HydA1 bound with [**2**]$^{-}$. The green trace corresponds to the sample prepared by incubating [**2**]$^{2-}$ with apo-HydA1 enzyme. The excess complex [**2**]$^{2-}$ was then removed by passing the sample through desalting column.

Cyclic Voltammogram

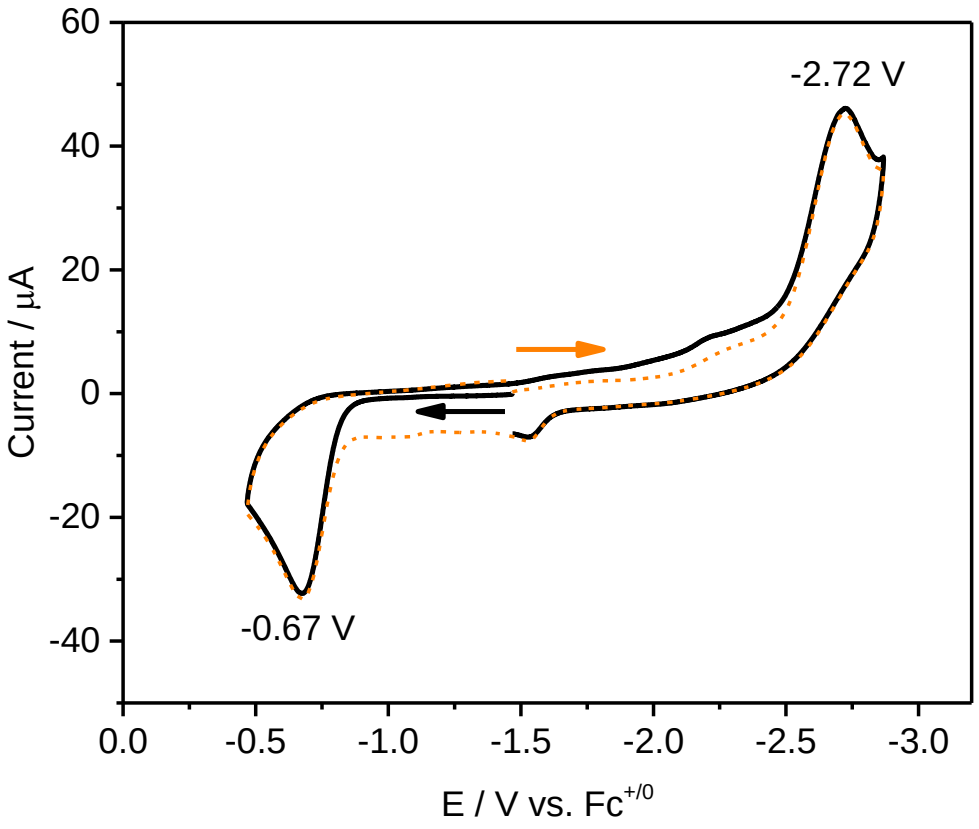

Figure S14. Cyclic voltammogram of $[K_2(18\text{-crown-6})_2(thf)][Fe_2(\mu\text{-}SH)_2(CN)_2(CO)_4]$ (1 mM) in acetonitrile (0.1 M $[NBu_4]PF_6$) under N_2. Black trace represents the scan direction to the positive potential first. Orange trace represents the scan direction to the negative potential first.

Computational Details

All calculations were performed using the ORCA quantum chemical program package v4.2.1.[15-16] Geometry optimizations and single-point property calculations were carried out with the BP86 functional,[17-18] which is tested to be an optimal functional for hydrogenase related diiron complexes.[19] In all cases, all-electron scalar-relativistic effects were included via the zeroth-order regular approximation (ZORA) formalism.[20-22] The calculations were accelerated by using RIJCOSX [23] (resolution of identity for the Coulomb part and a chain of spheres algorithm for the Hartree−Fock exchange part) approximations when appropriate. In geometry optimizations, tight optimization thresholds were employed and noncovalent interactions were considered via atom-pairwise dispersion corrections with Becke−Johnson (D3BJ) damping.[24-25] All optimized geometries are confirmed to be the local minimum via numerical frequency calculation.

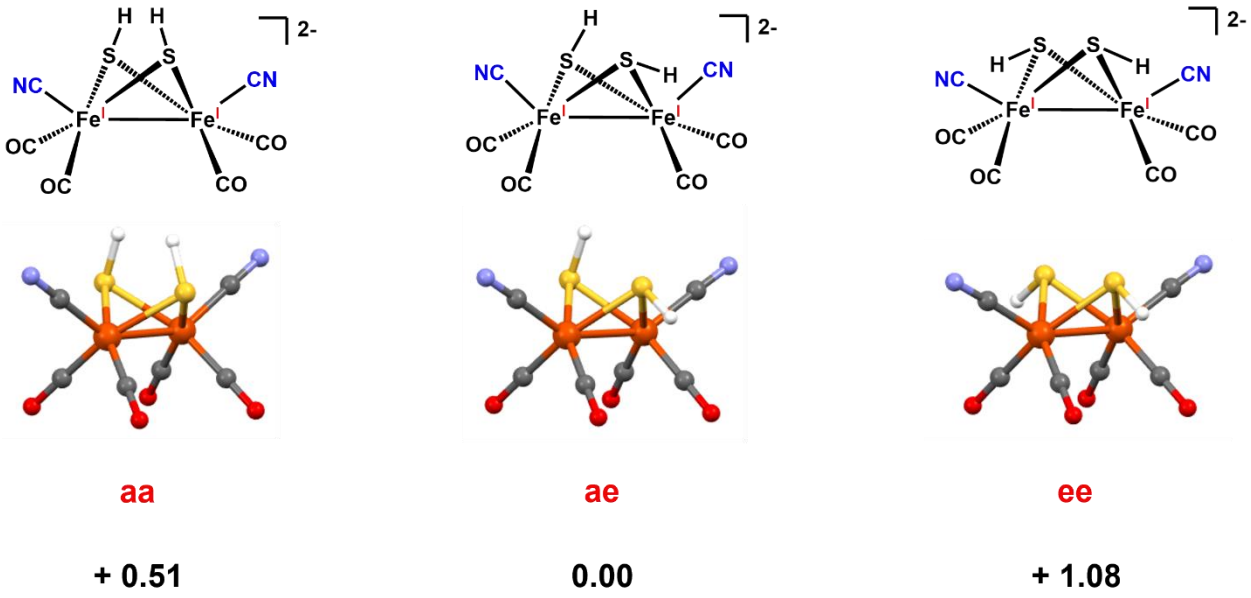

Figure S15. Comparison of the structures and relative Gibbs free energies from DFT calculation (black numbers, in kcal/mol) of the isomers for $[Fe_2(\mu\text{-}SH)_2(CN)_2(CO)_4]^{2-}$.

Input file examples

 # Single point calculation

!uks BP86 rijcosx tightscf slowconv zora zora-def2-tzvp sarc/j grid4 nofinalgrid gridx5 tightopt keepdens UCO UNO normalprint printbasis printmos CPCM(Acetonitrile) d3bj

%basis newgto Fe "ZORA-def2-qzvpp" end
end

%pal nprocs 16
end

%maxcore 3000

%scf MaxIter 500
end

*xyz -2 1
Coordinates.
*

 # Numerical frequency calculation

!uks bp86 rijcosx tightscf slowconv zora zora-def2-tzvp def2/J grid4 nofinalgrid gridx5 NumFreq normalprint printbasis printmos CPCM(Acetonitrile) d3bj

%basis newgto Fe "ZORA-def2-qzvpp" end
end

%pal nprocs 16
end

%freq CentralDiff true

Increment 0.01
end

%maxcore 3000

%scf MaxIter 500
end

*xyz -2 1
The coordinates from optimized geometry
*

Optimized geometries

Coordinates from ORCA-job FeSH_aa_bp86_ACN

Fe	0.33485882383755	3.50028276823307	5.91750567263257
Fe	-0.96182841251962	3.50048887546823	3.78358016987266
S	0.67671248335444	1.96803450618247	4.24895863746152
O	-0.96925603663850	5.56019365269743	7.50004534211170
O	-2.97037071720166	1.44089638694101	4.19912766147248
N	3.14439533189825	3.50180087979155	7.15899574321324
N	-0.75353754734834	3.50130820097131	0.71911329690643
C	-0.43058554271390	4.73710399265214	6.86410637376948
C	-2.15618086630534	2.26374554067830	4.01980945594658
C	2.06211009970267	3.50071424802143	6.69006800854006
C	-0.84310063277201	3.50069124021362	1.89522919045274
S	0.67691883049502	5.03264191896541	4.24912653588271
O	-0.96891523289712	1.43994921768833	7.49976196947698
O	-2.97002885617400	5.56053131063550	4.19835564514462
C	-0.43022115750974	2.26317112586228	6.86401602250266
C	-2.15597080375236	4.73744435251271	4.01952247439714
H	1.75359561243600	2.47868798890096	3.58835822360417

H	1.75369062410868	4.52176379958418	3.58852458761219

Coordinates from ORCA-job FeSH_ae_bp86_ACN

Fe	0.33566759565160	3.50838526485690	5.91048241945256
Fe	-0.96164600300052	3.50618231316909	3.77762118358168
S	0.74489597667642	2.02630688850401	4.20174678576141
O	-1.01598158841686	5.58459587544635	7.42272799645168
O	-2.94286128154203	1.43224280961318	4.23702047149554
N	3.10477202615413	3.53275016713213	7.24692879209589
N	-0.87052734518585	3.52507987480454	0.70427468913386
C	-0.46002380409904	4.74585248394010	6.82172901521877
C	-2.13563996827304	2.25875643956385	4.04057235788981
C	2.04093422206854	3.52233770414455	6.73740315197972
C	-0.90950683775478	3.51720831391329	1.88319189605935
S	0.77225994171277	4.95495912423863	4.18220961321490
O	-0.98311508469759	1.43392881057916	7.45751070361199
O	-2.93407241224213	5.57812367431212	4.26969439185251
C	-0.43789272068919	2.26096251745189	6.83139437134883
C	-2.14085326440790	4.74175370439358	4.05756562291898
H	1.80063437404793	2.59872331717155	3.55603467734928
H	0.20015665399755	6.13936702076501	4.52942182958318

Coordinates from ORCA-job FeSH_ee_bp86_ACN

Fe	0.34685970723760	3.49606075534395	5.89632228143992
Fe	-0.95087261844457	3.49647402295719	3.76807181225959
S	0.82542553555685	2.06847299166954	4.14396134908057
O	-1.01630925021158	5.56627002729613	7.40334990849927
O	-2.89367488860014	1.40131081515411	4.27037826554644
N	3.09446893486098	3.51198375309704	7.28294268237231
N	-0.93128072212694	3.50785511097743	0.69052093042008
C	-0.45487724322212	4.73239362844936	6.80036412397154

C	-2.10880823063420	2.24489820356124	4.05509304869790
C	2.04121001913539	3.50481751997687	6.75187661116817
C	-0.93771383980751	3.50291809707589	1.87007334274789
S	0.80774760411150	4.94305934959325	4.15522098709638
O	-0.98814699515149	1.39714935792473	7.38884131709090
O	-2.91830418059207	5.56637526945468	4.27881657184836
C	-0.43806315698110	2.24270651583094	6.79167786913913
C	-2.12358780615614	4.73286243850414	4.06045920730254
H	0.25156494246160	0.88968160436568	4.49589111359983
H	0.21911335656395	6.11161950176776	4.51662648471907

References

1. Kagalwala, H. N.; Lalaoui, N.; Li, Q.-L.; Liu, L.; Woods, T.; Rauchfuss, T. B., Redox and "antioxidant" properties of $Fe_2(\mu\text{-}SH)_2(CO)_4(PPh_3)_2$. *Inorg. Chem.* **2019,** *58* (4), 2761-2769.
2. Rao, G.; Britt, R. D., Electronic structure of two catalytic states of the [FeFe] hydrogenase H-cluster as probed by pulse electron paramagnetic resonance spectroscopy. *Inorg. Chem.* **2018,** *57* (17), 10935-10944.
3. Rao, G.; Pattenaude, S. A.; Alwan, K.; Blackburn, N. J.; Britt, R. D.; Rauchfuss, T. B., The binuclear cluster of [FeFe] hydrogenase is formed with sulfur donated by cysteine of an $[Fe(Cys)(CO)_2(CN)]$ organometallic precursor. *Proc. Natl. Acad. Sci. U.S.A* **2019,** *116* (42), 20850-20855.
4. Sun, L.; Bartlam, M.; Liu, Y.; Pang, H.; Rao, Z., Crystal structure of the pyridoxal-5'-phosphate-dependent serine dehydratase from human liver. *Protein Sci* **2005,** *14* (3), 791-798.
5. Bailey, L. B., *Folate in Health and Disease.* CRC Press: Boca Raton: 2009.
6. Stoll, S.; Schweiger, A., EasySpin, a comprehensive software package for spectral simulation and analysis in EPR. *J. Magn. Reson.* **2006,** *178* (1), 42-55.
7. Stoll, S.; Britt, R. D., General and efficient simulation of pulse EPR spectra. *Phys. Chem. Chem. Phys.* **2009,** *11* (31), 6614-6625.
8. Mims, W. B., Pulsed Endor Experiments. *Proceedings of the Royal Society of London. Series A. Mathematical and Physical Sciences* **1965,** *283* (1395), 452-457.
9. Davies, E. R., A New Pulse Endor Technique. *Phys. Lett.* **1974,** *47* (1), 1-2.
10. Bruggemann, W.; Niklas, J. R., Stochastic ENDOR. *J. Magn. Reson.* **1994,** *108* (1), 25-29.
11. Hoffman, B. M., Electron nuclear double resonance (ENDOR) of metalloenzymes. *Acc. Chem. Res.* **1991,** *24* (6), 164-170.
12. Rao, G.; Tao, L.; Britt, R. D., Serine is the molecular source of the $NH(CH_2)_2$ bridgehead moiety of the in vitro assembled [FeFe] hydrogenase H-cluster. *Chem. Sci.* **2020,** *11* (5), 1241-1247.
13. Myers, W. K.; Stich, T. A.; Suess, D. L. M.; Kuchenreuther, J. M.; Swartz, J. R.; Britt, R. D., The cyanide ligands of [FeFe] hydrogenase: pulse EPR studies of ^{13}C and ^{15}N-labeled H-cluster. *J. Am. Chem. Soc.* **2014,** *136* (35), 12237-12240.
14. Berggren, G.; Adamska, A.; Lambertz, C.; Simmons, T. R.; Esselborn, J.; Atta, M.; Gambarelli, S.; Mouesca, J. M.; Reijerse, E.; Lubitz, W.; Happe, T.; Artero, V.; Fontecave, M., Biomimetic assembly and activation of [FeFe]-hydrogenases. *Nature* **2013,** *499* (7456), 66-69.
15. Neese, F., Software update: the ORCA program system, version 4.0. *Wiley Interdiscip. Rev. Comput. Mol. Sci.* **2018,** *8* (1), e1327.
16. Neese, F., The ORCA program system. *Wiley Interdiscip. Rev. Comput. Mol. Sci.* **2012,** *2* (1), 73-78.
17. Perdew, J. P., Erratum: Density-functional approximation for the correlation energy of the inhomogeneous electron gas. *Phys. Rev. B* **1986,** *34* (10), 7406-7406.
18. Kassel, L. S., The Limiting High Temperature Rotational Partition Function of Nonrigid Molecules I. General Theory. II. CH_4, C_2H_6, C_3H_8, $CH(CH_3)_3$, $C(CH_3)_4$ and $CH_3(CH_2)_2CH_3$. III. Benzene and Its Eleven Methyl Derivatives. *J. Chem. Phys.* **1936,** *4* (4), 276-282.
19. Li, Q.; Lalaoui, N.; Woods, T. J.; Rauchfuss, T. B.; Arrigoni, F.; Zampella, G., Electron-rich, diiron bis(monothiolato) carbonyls: C–S bond homolysis in a mixed valence diiron dithiolate. *Inorg. Chem.* **2018,** *57* (8), 4409-4418.
20. Wüllen, C. v., Molecular density functional calculations in the regular relativistic approximation: Method, application to coinage metal diatomics, hydrides, fluorides and chlorides, and comparison with first-order relativistic calculations. *J. Chem. Phys.* **1998,** *109* (2), 392-399.

21. Lenthe, E. v.; Snijders, J. G.; Baerends, E. J., The zero-order regular approximation for relativistic effects: The effect of spin-orbit coupling in closed shell molecules. *J. Chem. Phys.* **1996,** *105* (15), 6505-6516.
22. Rolfes, J. D.; Neese, F.; Pantazis, D. A., All-electron scalar relativistic basis sets for the elements Rb–Xe. *J. Comput. Chem.* **2020,** *41* (20), 1842-1849.
23. Neese, F.; Wennmohs, F.; Hansen, A.; Becker, U., Efficient, approximate and parallel Hartree–Fock and hybrid DFT calculations. A 'chain-of-spheres' algorithm for the Hartree–Fock exchange. *Chem. Phys.* **2009,** *356* (1), 98-109.
24. Grimme, S.; Ehrlich, S.; Goerigk, L., Effect of the damping function in dispersion corrected density functional theory. *J. Comput. Chem.* **2011,** *32* (7), 1456-1465.
25. Grimme, S.; Antony, J.; Ehrlich, S.; Krieg, H., A consistent and accurate ab initio parametrization of density functional dispersion correction (DFT-D) for the 94 elements H-Pu. *J. Chem. Phys.* **2010,** *132* (15), 154104.